Article

Effect of Cr/Mn Addition in TiVNb on Hydrogen Sorption Properties: Thermodynamics and Phase Transition Study

Anis Bouzidi [1], Erik Elkaim [2] , Vivian Nassif [3] and Claudia Zlotea [1],*

1   Univ Paris Est Creteil, CNRS, ICMPE, UMR 7182, 2 rue Henri Dunant, 94320 Thiais, France; anis.bouzidi@cnrs.fr
2   Synchrotron SOLEIL, L'Orme des Merisiers, Saint-Aubin, 91192 Gif sur Yvette, France; erik.elkaim@synchrotron-soleil.fr
3   University Grenoble Alpes, CNRS, Institut Néel, 38000 Grenoble, France; nassif@ill.fr
*   Correspondence: claudia.zlotea@cnrs.fr

Abstract: High-entropy alloys (HEAs) are a promising class of materials that can grant remarkable functional performances for a large range of applications due to their highly tunable composition. Among these applications, recently, *bcc* HEAs capable of forming *fcc* hydrides have been proposed as high-capacity hydrogen storage materials with improved thermodynamics compared to classical metal hydrides. In this context, a single-phase *bcc* $(TiVNb)_{0.90}Cr_{0.05}Mn_{0.05}$ HEA was prepared by arc melting to evaluate the effect of combined Cr/Mn addition in the ternary TiVNb. A thermodynamic destabilization of the *fcc* hydride phase was found in the HEA compared to the initial TiVNb. In situ neutron and synchrotron X-ray diffraction experiments put forward a *fcc* → *bcc* phase transition of the metallic subnetwork in the temperature range of 260–350 °C, whereas the H/D subnetwork underwent an order → disorder transition at 180 °C. The absorption/desorption cycling demonstrated very fast absorption kinetics at room temperature in less than 1 min with a remarkable total capacity (2.8 wt.%) without phase segregation. Therefore, the design strategy consisting of small additions of non-hydride-forming elements into refractory HEAs allows for materials with promising properties for solid-state hydrogen storage to be obtained.

Keywords: high-entropy alloys; hydrogen storage; in situ synchrotron X-ray diffraction; in situ neutron diffraction

1. Introduction

The shift towards a cleaner energy sector has become crucial to reduce the dependence on fossil fuels and reach zero net emissions. The transition to low-carbon energy could be achieved by relying on hydrogen due to its strong and promising potential as an alternative fuel of the future [1–4]. Nevertheless, the practical deployment of hydrogen as a safe, compact, and low-cost energy carrier remains a challenge. The most mature storage technologies for hydrogen are compressed gas in high-pressure cylinders and cryogenic liquid. However, these forms of storage result in cost and safety issues [2,5]. A viable alternative form of storage is solid-state storage based on hydride-forming materials with tunable operating conditions. In this regard, interstitial metal hydrides showed interesting performances for various types of applications. The hydrogen sorption properties can be tuned by controlling the chemical composition of the alloys/intermetallics, but their practical application is limited by a relatively small storage capacity, activation issues, and cycle–life instability [6,7].

In this context, high-entropy alloys (HEAs), as materials containing at least five principal elements with the concentration of each element between 5 and 35 at.%, have been proposed to alleviate the drawbacks of conventional alloys. The multicomponent nature and, consequently, the high entropy of mixing lead to the formation of solid solutions with simple crystalline structures, such as body-centered cubic (*bcc*), face-centered cubic

(*fcc*), and hexagonal close-packed (*hcp*) [8–12]. In recent years, HEAs containing refractory elements have been studied regarding their hydrogen sorption properties [13–17]. The multicomponent alloying strategy enables the exploration of a vast compositional space to optimize the hydrogen storage capacity and tailor thermodynamics to ambient conditions. Since refractory metals are known to easily absorb hydrogen forming hydrides with a high storage capacity, most reports focused on refractory-containing HEAs with very promising performances [8–10]. Despite these encouraging results, thermodynamics need improvement, as many of these refractory HEAs show very stable hydrides that require high temperatures for the full recovery of hydrogen [18]. Recently, a thermodynamic model to calculate PCT diagrams for *bcc* multicomponent alloys has been successfully proposed and implemented in open-source code with a user-friendly interface [19–21].

In this study, our interest focuses on the ternary TiVNb alloy, which crystalizes in a single-phase *bcc* lattice ($Im\bar{3}m$) and reaches a maximum capacity of hydrogen storage of 2 H/M (3.2 wt.%), forming an *fcc* dihydride phase ($Fm\bar{3}m$). The high hydrogen storage capacity explains the large interest in this composition [14,15,17]. Despite its high storage capacity and very fast kinetics, this alloy forms a very stable dihydride at room temperature (with a very low equilibrium plateau pressure at 25 °C and a high temperature for hydrogen desorption). Consequently, previous studies reported the influence of the addition of non-hydride-forming elements in TiVNb on the thermodynamic properties of related hydrides. Strozi et al. extensively studied the series of $(TiVNb)_{100-x}Cr_x$ alloys (x = 0, 15, 20, 25, 30, 35, 40) [22–24]. Interestingly, the addition of Cr up to 35 at.% into the ternary TiVNb alloy leads to the formation of single-phase *bcc* materials with reduced lattice parameters. However, the richest Cr composition (40 at.%) is mainly composed of the C15 cubic Laves phase. The addition of Cr influences the hydrogen storage capacity, which slightly decreases from 2 to 1.76 H/M for TiVNb and $(TiVNb)_{65}Cr_{35}$, respectively. The hydrides of $(TiVNb)_{100-x}Cr_x$ alloys (x = 0, 15, 20, 25, and 30) are pure *fcc* phases, whereas the $(TiVNb)_{65}Cr_{35}$ hydride is a mixture of *fcc* and *bcc* phases. Furthermore, Cr addition demonstrates a thermodynamic destabilization of the hydride formation, which results in an increase in the equilibrium pressure compared to the pristine alloy. However, our main interest is in comprehending the role of Cr addition to TiVNb by limiting the added content and achieving optimal hydrogen sorption properties.

Following the same methodology, Ferreira et al. investigated the effect of simultaneously adding two non-hydride-forming elements, Cr and Al, into the TiVNb alloy by studying the following series: $(TiVNb)_{100-x}(CrAl)_x$ (x = 10, 20, 30, and 40) [25]. The authors' strategy was to destabilize the hydride formation and improve the storage capacity. All of the alloys crystallize in a *bcc* phase with a small fraction of a secondary phase in the alloys with 20 and 40 at.% of Cr and Al. The addition of Cr and Al reduced the lattice parameter of the TiVNb alloy. Similarly to the previous study by Strozi et al., a significant decrease in the hydrogen storage capacity was demonstrated from 2 H/M for TiVNb to 0.41 H/M when x = 40. The hydride phases were dependent on the amount of Cr and Al: for x = 10, the alloy can fully transform into an *fcc* hydride phase; on the contrary, for x = 20, the alloy forms an incomplete hydride with a mixture of a body-centered tetragonal (*bct*) and a *bcc* phases; finally, for x = 30 and 40, the alloys could only partially absorb hydrogen and transform into a *bcc* monohydride. Interestingly, the thermodynamic properties of the TiVNb were strongly influenced by the addition of Cr and Al, leading to a destabilization of hydride formation up to x = 20 (10 at.% Al and 10 at.% Cr). Moreover, when comparing the thermodynamic properties of previously reported alloys, such as $TiVNbCr_x$ [24] and Al_xTiVNb [26], a stronger destabilization is observed when using a combination of two non-hydride-forming elements, such as Cr and Al in TiVNb.

Recently, Serrano et al. investigated the structural and hydrogen properties of a series of alloys: $Ti_{35}V_{35}Nb_{20}Cr_5Mn_5$, $Ti_{32}V_{32}Nb_{18}Cr_9Mn_9$, and $Ti_{27.5}V_{27.5}Nb_{20}Cr_{12.5}Mn_{12.5}$ [27]. The three alloys were synthesized by arc melting and formed a *bcc* single phase, except for the alloy containing the highest amounts of Cr and Mn ($Ti_{27.5}V_{27.5}Nb_{20}Cr_{12.5}Mn_{12.5}$), which formed a main *bcc* phase with a secondary C14 Laves phase (7% phase fraction). At room

temperature, the $Ti_{35}V_{35}Nb_{20}Cr_5Mn_5$ and $Ti_{32}V_{32}Nb_{18}Cr_9Mn_9$ showed a small incubation time followed by slow kinetics of hydrogen absorption for a final storage capacity of 2.47 and 2.09 wt.%, respectively. Interestingly, the alloy containing the highest amount of Cr and Mn showed an incubation time of 450 min, which was followed by a fast absorption rate, achieving the highest capacity of hydrogen storage of 3.38 wt.%. The $Ti_{35}V_{35}Nb_{20}Cr_5Mn_5$ and $Ti_{32}V_{32}Nb_{18}Cr_9Mn_9$ formed an *fcc* hydride phase with a small fraction of a *bcc* phase, which indicates an incomplete hydrogenation of the samples. Furthermore, the hydride phase of the $Ti_{27.5}V_{27.5}Nb_{20}Cr_{12.5}Mn_{12.5}$ alloy was a pure *fcc* phase.

These previous studies highlighted that the addition of Al, Cr, and Mn to the ternary TiVNb alloy can upgrade the hydrogen sorption properties. Nevertheless, a limited stoichiometry of additional elements must be followed to obtain initial single-phase *bcc* alloys with high hydrogen absorption capacity.

For all the above-mentioned reasons, the aim of this study is to investigate the simultaneous addition of 5 at.% Cr and 5 at.% Mn into the TiVNb alloy. This report details the investigation of the $Ti_{0.30}V_{0.30}Nb_{0.30}Mn_{0.05}Cr_{0.05}$ high-entropy alloy regarding the synthesis and characterization of the physicochemical and hydrogen sorption properties with the help of laboratories and large-scale facilities. To highlight the chemical composition effect on hydrogen sorption performances, a thorough comparison with previous results obtained by the addition of other elements to the TiVNb alloy will be carried out.

2. Materials and Methods

The $Ti_{0.30}V_{0.30}Nb_{0.30}Mn_{0.05}Cr_{0.05}$ alloy was synthesized by arc melting under an Ar atmosphere to avoid contamination. The alloy was produced by melting Ti, V, Nb, and Cr pieces six times to form a quaternary pre-alloy, followed by the addition of Mn pieces. The final alloy was melted three times to obtain the desired chemical composition.

The crystalline structure was studied by X-ray powder diffraction (XRD) using both laboratory X-ray diffractometer D8 advance Bruker (Cu K_α radiation (λ = 1.5406 Å), Bragg-Brentano geometry) and synchrotron radiation measurements (SR-XRD) at the CRISTAL beamline in SOLEIL facility. Ex situ and in situ (λ = 0.67156 Å) SR-XRD diagrams were recorded using the Mythen2 detector system (Dectris Ltd., Baden-Daettwil, Switzerland) installed on the powder diffractometer. To minimize X-ray absorption, samples were mixed with a fumed silica powder and enclosed in quartz capillary tubes that are 0.22 mm in diameter. The SR-XRD patterns were recorded during hydrogen desorption by applying a constant temperature ramp from 25 to 450 °C (2 °C/min) under a secondary vacuum. The scanning range was from 0.2° to 65° (2 θ) within a 3 minute acquisition time per scan.

Powder neutron diffraction experiments on deuterated samples were performed at the D1B beamline (λ = 1.28 Å) at the Institute Laue-Langevin, Grenoble, France (DOI: 10.5291/ILL.DATA.CRG-2768), in the scanning range from 1 to 128° (2θ). At room temperature, the ex situ measurement was carried out in a vanadium container, whereas for the in situ acquisitions, the sample was placed in a silica tube connected to vacuum equipment (base pressure~10^{-5} mbar). The diffraction patterns were recorded during the desorption of the deuterium by applying constant heating (1 °C/min) under a secondary vacuum. The pressure of the evolved gas was continuously recorded by a vacuum gauge during the desorption experiment.

The microstructure of the as-cast and the cycled materials was investigated by scanning electron microscopy (SEM) using a Zeiss Merlin microscope. The samples were immobilized in epoxy resin and coated with 1.9 nm of Pd. The chemical mapping was analyzed by energy dispersive X-ray spectroscopy (EDS). The values of the chemical composition have been obtained by taking the average of 5 and 10 large areas in different positions on the sample.

The refinements of ex situ neutron and SR powder diffraction data were carried out using the Rietveld method with Fullprof software [28], whereas Le Bail refinement [29] was preferred for the structural analysis of in situ neutron and SR diffraction experiments. The fundamental parameters approach, as implemented in the TOPAS program (Bruker AXS

version 7.0.0.7), was used to refine the structural model parameters of the laboratory X-ray diffraction patterns [30,31].

Hydrogen sorption properties were studied using a homemade volumetric device thermalized at 25 °C. Small pieces of the as-cast alloy were loaded in a tight stainless-steel container. Prior to the first absorption of hydrogen, the sample was activated by a heat treatment at 350 °C under dynamic vacuum for 3 h. The hydrogen uptake was calculated using the real equation of state for hydrogen from the GASPAK V3.32 database (Cryodata Inc., Littleton, CO, USA). Pressure Composition Isotherms (PCI) at 133, 158, and 208 °C have been acquired and further used to calculate the enthalpy and entropy of the reaction using the Van't Hoff equation (Equation (1)) [32].

$$\ln(p_{eq}/p_0) = \Delta H/RT - \Delta S/R \qquad (1)$$

Absorption/desorption cycling measurements were recorded using the same volumetric device, starting with a material that has been activated by one hydrogen absorption/desorption step. The absorption was performed under 25 bar H_2 pressure at 25 °C, while the desorption was carried out by heating at 400 °C under dynamic vacuum for 12 h. During the absorption step at 25 °C, the kinetic curves were recorded.

3. Results

The as-cast $(TiVNb)_{0.90}Mn_{0.05}Cr_{0.05}$ alloy is a single-phase *bcc* material ($Im\bar{3}m$) with a lattice parameter of 3.194(1) Å, as demonstrated by powder SR-XRD (Figure 1 and Table 1). For the sake of comparison, Table 1 lists the lattice parameters of closely related TiVNb-based compositions from the literature [14,25,26]. This lattice parameter value is inferior to 3.211 Å obtained for the ternary TiVNb alloy and closely related to other compositions in this alloy family (Table 1). A reduced lattice parameter can be explained by the decrease in the average atomic radius in the presence of 5 at.% Cr and 5 at.% Mn (1.388 Å), as compared to the initial ternary alloy (1.395 Å), due to the small atomic radius for both additional metals ($r_{Cr} = 1.25$ Å $< r_V = 1.31$ Å $< r_{Mn} = 1.37$ Å $< r_{Nb} = 1.43$ Å $< r_{Ti} = 1.45$ Å) [33].
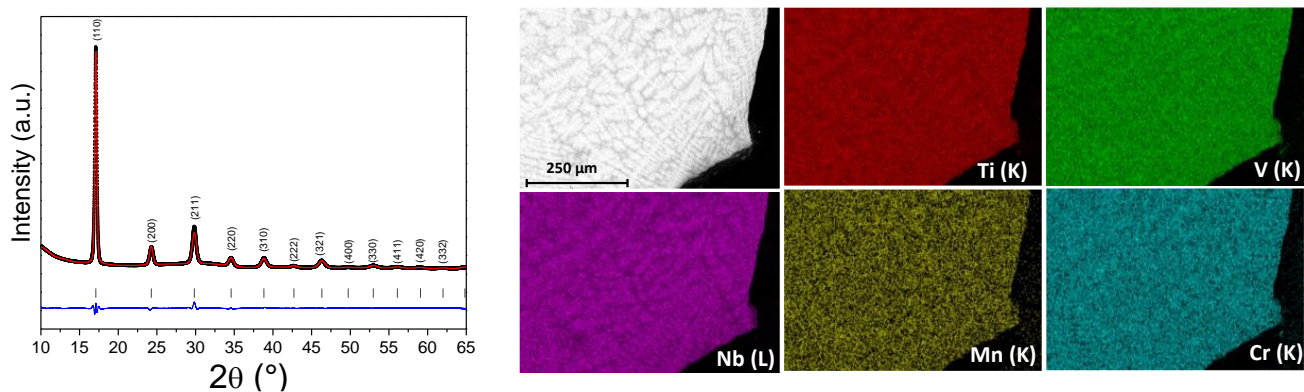

Figure 1. SR-XRD pattern and corresponding Rietveld refinement ($\lambda = 0.67156$ Å) (**left**) and SEM-EDX chemical mapping (**right**) of the $(TiVNb)_{0.90}Cr_{0.05}Mn_{0.05}$ alloy.

Table 1. Physicochemical (lattice type, space group, lattice parameter, and bulk density) and thermodynamic properties (entropy and entropy of hydride formation) for $(TiVNb)_{0.90}Mn_{0.05}Cr_{0.05}$ and related TiVNb-based compositions from references [26,34,35].

Composition	Lattice	SG	a (Å)	Density (g/cm^3)	ΔH_{abs} (kJ/molH$_2$)	ΔS_{abs} (J/K·molH$_2$)	Ref.
TiVNb			3.211	6.42	-	-	[34]
$(TiVNb)_{0.90}Cr_{0.05}Mn_{0.05}$			3.194(1)	6.41	-	-	Present work
$(TiVNb)_{0.90}Cr_{0.05}Al_{0.05}$			3.190	6.29	-	-	[26]
$(TiVNb)_{0.80}Cr_{0.10}Al_{0.10}$	*bcc*	$Im\bar{3}m$	3.162	6.2	-	-	[26]
$(TiVNb)_{0.90}Al_{0.05}Mo_{0.05}$			3.201	6.4	-	-	[35]
$(TiVNb)_{0.90}Al_{0.10}$			3.197	6.1	-	-	[34]
$(TiVNb)_{0.95}Al_{0.05}$			3.203	6.3	-	-	[26]
$(TiVNb)H_2$			4.443	-	−67	−157	[34]
$(TiVNb)_{0.90}Cr_{0.05}Mn_{0.05}H_{1.96}$			4.412(1)	-	−63.5(1)	−153(3)	Present work
$(TiVNb)_{0.90}Cr_{0.05}Al_{0.05}H_{1.8}$	*fcc*	$Fm\bar{3}m$	4.399	-	−49	−139	[26]
$(TiVNb)_{0.90}Al_{0.05}Mo_{0.05}H_{1.8}$			4.408	-	−45	−139	[35]
$(TiVNb)_{0.90}Al_{0.10}H_{1.6}$			4.376	-	−49	−154	[34]
$(TiVNb)_{0.95}Al_{0.05}H_{1.8}$			4.418	-	−52	−141	[26]
$(TiVNb)_{0.80}Cr_{0.10}Al_{0.10}H_{1.4}$	*bct*	$I4/mmm$	a = 3.067 c = 4.263	-	−34	−130	[26]

The alloy is chemically homogenous, and the overall chemical composition is very close to the nominal one, as proven by SEM-EDX (Figure 1 and Table 2). A dendritic microstructure can be noticed, which is typical for high-entropy alloys [36,37]. As expected, the dendritic areas are enriched in Nb, whereas the interdendritic regions contain slightly more Ti and V than the average composition (Table 2).

Table 2. SEM-EDX chemical mapping results of the as-cast $(TiVNb)_{0.9}Cr_{0.05}Mn_{0.05}$ alloy.

Region	Ti (at.%)	V (at.%)	Cr (at.%)	Mn (at.%)	Nb (at.%)
Dendritic	29.8 (0.8)	29.7 (0.6)	4.4 (0.6)	4.0 (0.9)	32.1 (1.7)
Interdendritic	30.6 (1.1)	30.7 (0.9)	5.4 (0.5)	5.1 (1.0)	28.2 (0.7)
Overall	29.9 (0.2)	29.8 (0.3)	5.1 (0.3)	5.0 (0.4)	30.2 (0.2)
Nominal	30	30	5	5	30

The bulk density is almost unchanged from 6.42 to 6.41 g/cm^3 by Cr/Mn addition; thus, the $(TiVNb)_{0.90}Cr_{0.05}Mn_{0.05}$ material can be considered a *bcc* single-phase lightweight refractory high entropy alloy, as defined previously [12,38].

The hydrogen absorption PCI measurements at several temperatures (Figure 2) reveal that this composition undergoes a two-step reaction with hydrogen from the initial alloy to an intermediate monohydride (capacity~1 H/M) at very low pressure and finally to a dihydride phase (capacity~2 H/M) at higher pressures, as also noticed for the ternary alloy [34] and many similar materials [39,40]. The corresponding Van't Hoff plot is inserted in Figure 2, and the thermodynamic values for the hydride formation are the following: $\Delta H_{abs} = -63.5 (\pm 1.0)$ kJ/molH_2 and $\Delta S_{abs} = -153 (\pm 3)$ J/K·mol H_2. The latter is close to the expected value of the free H_2 gas entropy (130 J/K·mol H_2). The enthalpy of hydride formation of the present alloy (-63.5 kJ/mol H_2) is smaller than the initial ternary TiVNb composition (-67 kJ/mol H_2), pointing out a destabilization of the hydride formation by 5 at.% Cr/5 at.% Mn addition.
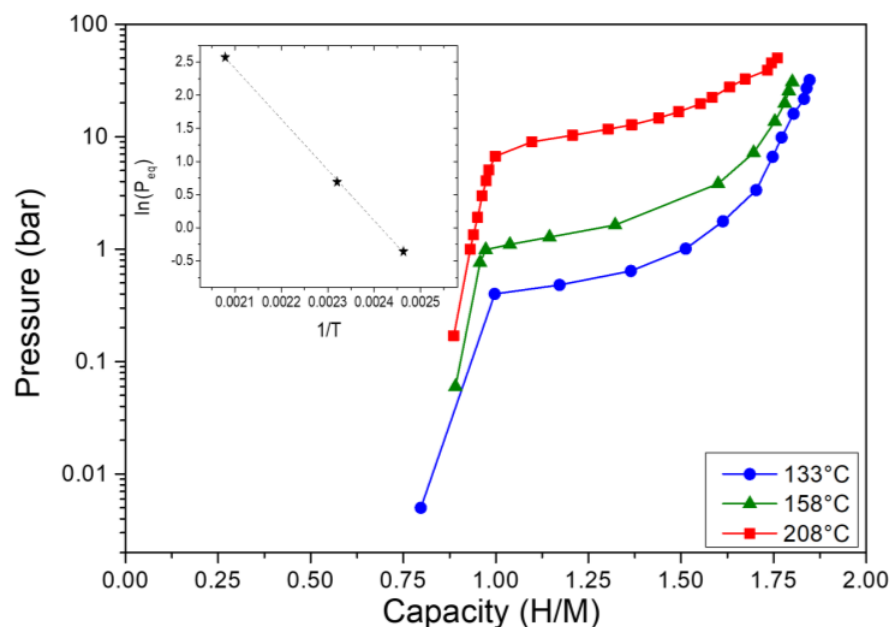

Figure 2. Pressure−composition−isotherms during hydrogen absorption at different temperatures for the $(TiVNb)_{0.90}Cr_{0.05}Mn_{0.05}$ alloy. The Van't Hoff plot is also inserted.

A comparison between the enthalpy of hydride formation and related systems previously reported is given in Table 1 and Figure 3.
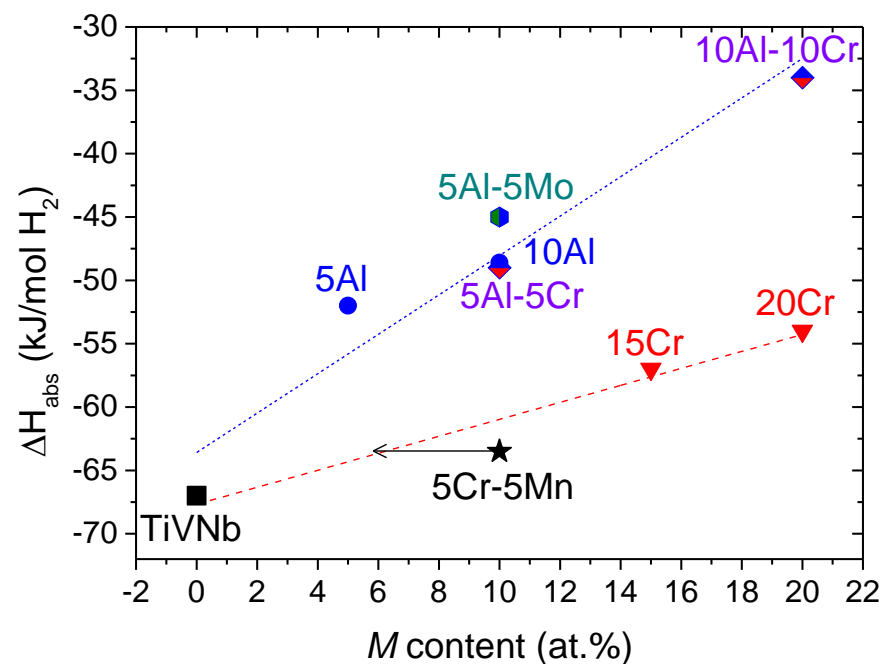
Figure 3. The enthalpy of hydride formation (ΔH_{abs}) in the equimolar TiVNb alloy (square) as a function of additional elements M (at.%): Cr_x(TiVNb) [26] (triangles), $(Al/Cr)_x$(TiVNb) [27] (diamonds), Al_x(TiVNb) [28] (circles), and $(Al/Mo)_x$(TiVNb) (hexagon). The present alloy is represented as a black star. The dotted linear fits are plotted as guides for the eye.

Two main families of alloys can be distinguished in Figure 3, illustrated as two dotted lines. The Cr_x(TiVNb) system shows an almost linear variation of the enthalpy of hydride formation with Cr content but with a smaller slope than the Al-containing alloys. It is obvious that the thermodynamics of the present alloy are altered mainly by the presence of Cr since it aligns well with the trend for the Cr_x(TiVNb) family and agrees with the value expected at around 5–6 at.% Cr (see the arrow in Figure 3). From this observation, it seems that Cr plays a major role in thermodynamic destabilization. For the sake of clarity, it is worth mentioning that the enthalpy of hydride formation for the composition with 5 at.% Cr has not been reported in the literature. However, a closer inspection of Figure 3 highlights that Al has a stronger role in the thermodynamic destabilization than Cr, as the linear trend shows a higher slope. This destabilization is not only more significant than Cr, but it also seems that the presence of Al is the most important, irrespective of composition. However, this destabilization occurs at the expense of storage capacity, which decreases more notably in the presence of Al atoms than Cr/Mn. The present alloy shows a maximum storage capacity of 1.96 H/M, which is higher than the 1.8–1.2 H/M observed in all Al-containing alloys (Table 1). This simple comparison allows us to set the following scale affecting the thermodynamics of hydride formation in TiVNb-related compositions: Mn < Cr < Al. These differences might be related to electronic effects at the atomic scale that can be highlighted by ab initio DFT calculations in the future.

The $(TiVNb)_{0.90}Cr_{0.05}Mn_{0.05}$ alloy was fully hydrogenated/deuterated at room temperature, and the maximum capacity obtained was close to 2 H(D)/M. The crystalline structure of the full hydrogenated/deuterated alloy was determined by SR-XRD (Figure 4a) and neutron diffraction (Figure 4b), respectively.
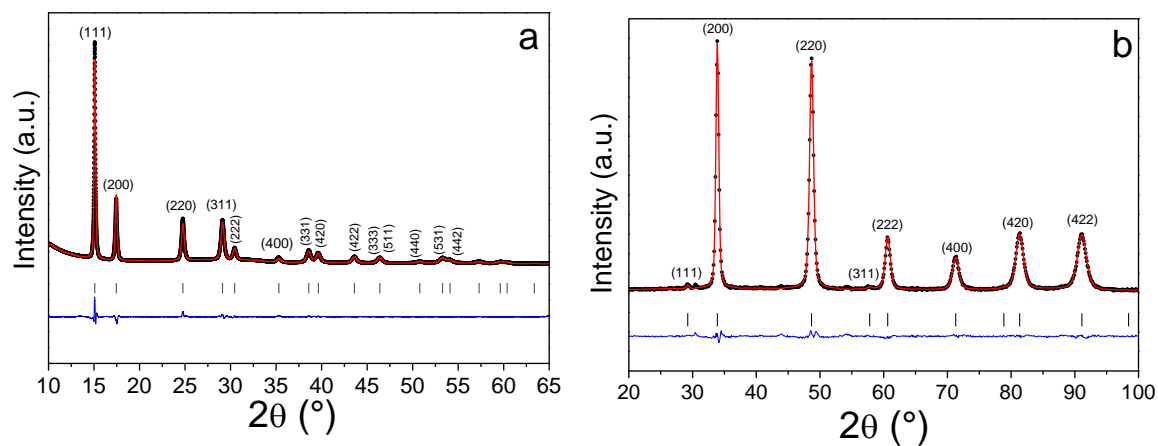
Figure 4. Powder SR-XRD (λ = 0.67156 Å) (**a**) and neutron diffraction (λ = 1.28 Å) (**b**) patterns of the $(TiVNb)_{0.90}Cr_{0.05}Mn_{0.05}H_2/D_2$, respectively, with the corresponding Rietveld refinements.

Since the interactions between the material and X-rays or neutrons are different, the two diagrams give access to complementary information: XRD reveals the metallic subnetwork since H/D cannot be detected by this method, whereas neutron diffraction mainly gives information about the deuterium subnetwork since the coherent scattering length of the metallic subnetwork is very small, around +1 fm, as compared to the respective deuteride +14.3 fm. The SR-XRD on the full hydride reveals that the metal subnetwork adopts an *fcc* lattice, whereas neutron diffraction highlights the location of hydrogen/deuterium in the tetrahedral interstitial sites (¼, ¼, ¼) of the *fcc* structure.

Once the structure of fully hydrogenated/deuterated material was confirmed, the thermal desorption of hydrogen/deuterium was studied by in situ neutron diffraction (Figure 5) and SR-XRD (Figure 6) during heating with a constant ramp of 1 °C/min and 2 °C/min, respectively, under dynamic secondary vacuum. The diffraction peaks from the ordered deuterium atoms in the tetrahedral sites of the *fcc* lattice are visible in the neutron thermo-diffractograms (Figure 5 left-hand) together with the profile of gas desorption recorded during the experiment (middle panel of Figure 5), whereas the thermal evolution of the *fcc* lattice parameter, as obtained by Le Bail fitting, is shown in the right-hand panel.
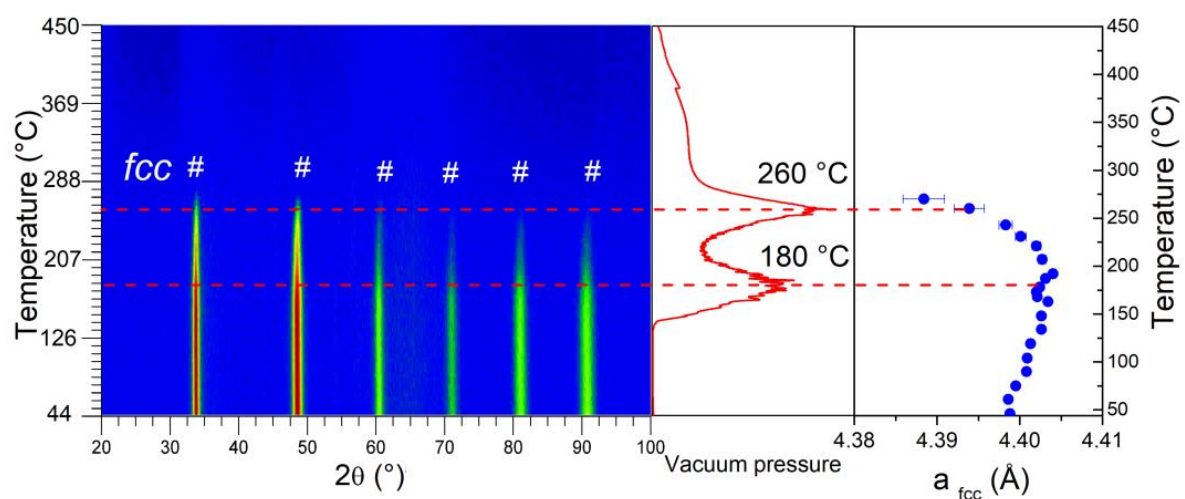

Figure 5. Left-hand panel: in situ neutron thermo-diffraction of $(TiVNb)_{0.90}Cr_{0.05}Mn_{0.05}D_2$ during heating under dynamic vacuum with 1 °C/min (λ = 1.28 Å) (fcc deuteride phase is marked with #). Middle panel: gas desorption profile. Right-hand panel: thermal evolution of the *fcc* lattice parameter (marked with blue dots).
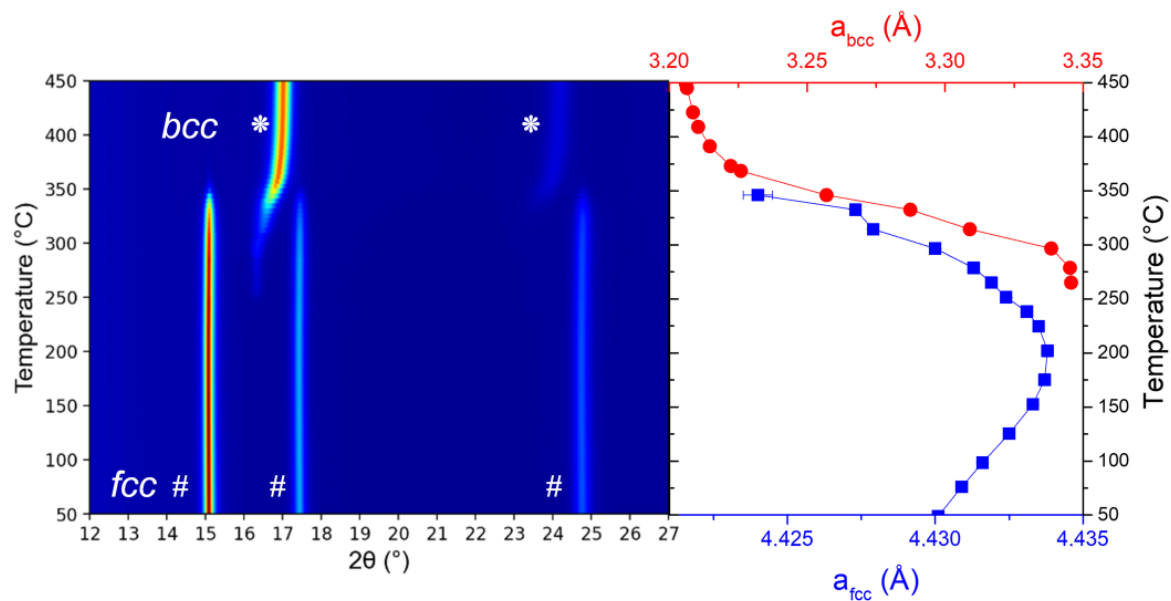
Figure 6. Left-hand panel: in situ SR-XRD $(TiVNb)_{0.90}Cr_{0.05}Mn_{0.05}H_2$ during heating under dynamic vacuum at 2 °C/min ($\lambda = 0.67156$ Å). Right-hand panel: thermal evolution of the *fcc* (marked with blue symbols) and *bcc* (marked with red symbols) lattice parameters.

The intensity of the *fcc* diffraction peaks is stable up to around 150 °C, with a small increase in the lattice parameter (right-hand panel), probably due to the thermal expansion effect. In the 150–200 °C range, the lattice parameter stabilizes while the first desorption event occurs at 180 °C (middle panel). The diffraction peaks progressively fade in the range of 200–260 °C and completely vanish above this temperature. The latter value corresponds to the second main desorption event, while the lattice parameter experiences a strong decrease above 260 °C. The desorption profile above this temperature demonstrates a continuous plateau-like event that finishes at around 450 °C (middle panel), whereas diffraction peaks are not visible in this range. This hints at a disordered deuterium arrangement in the interstitial sites of the solid phase in this temperature range. The presence of random deuterium atoms in the solid phase is corroborated by the variation of the background level between 5–6° (2θ) far from any diffraction peaks (Figure S1). This approach was proposed to explain the correlations between the disordered deuterium atoms inside the interstitial sites and the neutron diffraction background level in metal deuterides [16]. In the present case, the background intensity is stable up to around 150 °C, which corresponds to the initiation of the desorption, then decreases steadily up to 350 °C. Above this threshold, a plateau-like pattern is observed, suggesting that most deuterium atoms are desorbed and their contribution to the diffraction background is negligible.

The metallic subnetwork thermal behaviour is shown in Figure 7, together with the evolution of the lattice parameters for both *fcc* and *bcc* phases, as determined by Le Bail fitting.

Similarly, the *fcc* diffraction peaks are visible at low temperatures up to around 260 °C, where the desorbed *bcc* phase starts to appear. Since XRD reveals mainly the metallic subnetwork, the emergence and evolution of the desorbed *bcc* phase are now possible. The *fcc* phase disappears above 350 °C, while the *bcc* desorbed phase reinforces. The *fcc* lattice parameter steadily increases with temperature up to around 150 °C, where a decrease is initiated and progressively continues up to 350 °C. The *bcc* phase appears at around 260 °C, and the related lattice parameter is stable up to 280 °C. Above this threshold, it starts to sharply decrease up to 450 °C, where a stabilization seems to be reached.
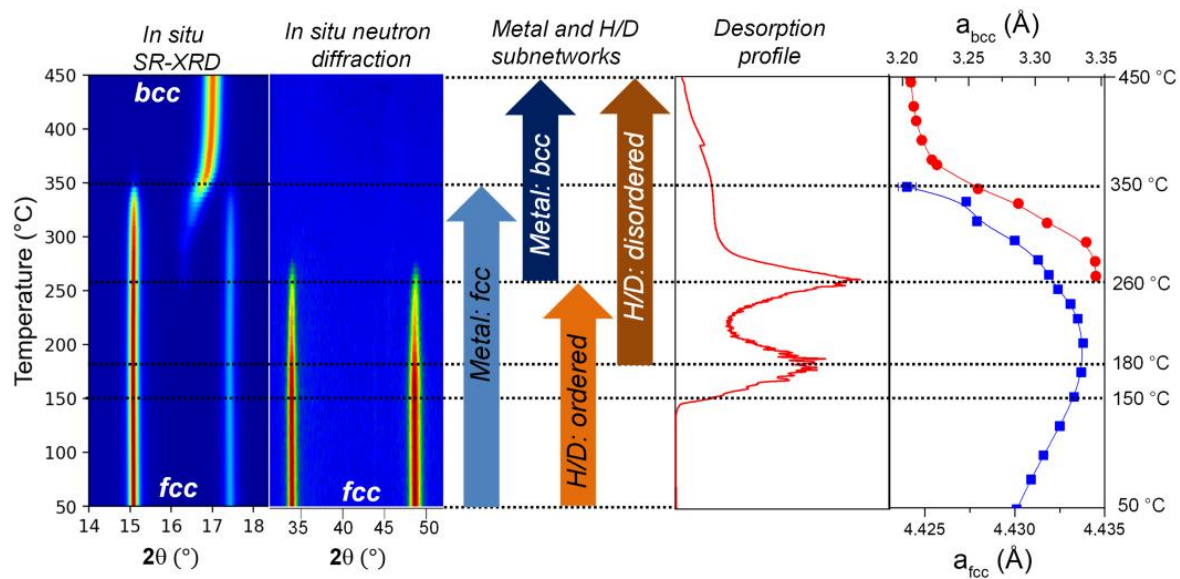
Figure 7. Synthesis of combined synchrotron X-ray and neutron diffraction results reveal the "metal" and "H/D" subnetworks phase transformation during the thermo-desorption of $(TiVNb)_{0.90}Cr_{0.05}Mn_{0.05}H/D_2$. The right-hand panel corresponds to SR-XRD analysis.

Both in situ neutron and synchrotron radiation experiments are in good agreement: the desorption starts at around 150 °C, where the linear expansion of the *fcc* lattice parameter slows down concomitantly to the first desorption event observed in the gas evolution profile at around 180 °C (middle panel of Figure 5). Above this temperature, the *fcc* lattice parameter diminishes until the phase completely disappears at 260 °C and 350 °C for neutron diffraction and SR-XRD, respectively. The value of 260 °C noticed for the vanishing of the *fcc* phase in neutron diffraction corroborates the second desorption event in the gas evolution profile (middle panel of Figure 5). The difference in these temperature thresholds related to the vanishing of the *fcc* phase can be explained by the interaction of neutrons/X-rays with the material. The remaining deuterium atoms in the 260–350 °C range might still be present in the *fcc* phase but highly disordered, which justifies the absence of diffraction peaks in neutron diffraction but the presence of peaks in SR-XRD patterns. Above 350 °C, the *bcc* phase is only present in the SR-XRD and absent in neutron diffraction patterns, and this has been accounted for by the extremely small coherent scattering length of the pure metallic subnetwork together with the disordered D subnetwork in the *bcc* phase. We hypothesize that this behaviour is inherited from the disordered D subnetwork in the *fcc* phase at lower temperatures. This thermal behaviour is in agreement with closely related materials [34]. Interestingly, the first desorption peak in the desorption profile does not relate to a phase transition as suggested earlier [41] but to a more subtle transformation that prompts an order/disorder change in the D subnetwork. On the contrary, the second desorption event at 260 °C is clearly due to the *fcc*-to-*bcc* phase transition.

The lattice parameter of the full desorbed *bcc* phase is around 3.206 Å at 450 °C, which is slightly larger than 3.194 Å at room temperature for the pristine alloy, but this can be explained by the temperature difference and dilatation of the lattice at high temperature.

In summary, the in situ experiments revealed an interesting thermal effect in the diffraction patterns that can be understood by a specific interaction between the probe beam (neutron or X-ray) and the deuterium/metals in the material. Consequently, we propose the following transformations during the thermo-desorption experiments, as comparatively illustrated in Figure 7:

(i)   50–150 °C: the *fcc* phase is stable while the lattice parameter expands linearly with the temperature;

(ii) 150–180 °C: the desorption starts at around 150 °C with a first main event at 180 °C that decelerates the expansion of the *fcc* lattice parameter;

(iii) 180–260 °C: the *fcc* lattice parameter strongly decreases together with an order → disorder transition of the H/D subnetwork noticeable as vanishing of the intensity of the *fcc* phase in neutron diffraction;

(iv) 260 °C: a second main desorption event occurs, which marks the beginning of the *fcc* → *bcc* phase transition, as discernible in SR-XRD, whereas no diffraction peaks are detectable in neutron diffraction patterns;

(v) 260–350 °C: the phase transition continues; both phases coexist while their lattice parameters strongly decline. The remaining H/D atoms are randomly distributed in the interstitial sites;

(vi) 350 °C: the *fcc* phase disappears and only the *bcc* one is noticeable in SR-XRD while the remaining H/D atoms progressively desorb with a plateau-like desorption event;

(vii) 350–450 °C: the *bcc* lattice parameter decreases less drastically than before;

(viii) 450 °C: full desorption and lattice parameter stabilization are reached.

These results demonstrate that the hydrogen absorption and desorption in this alloy are reversible, and consequently, it can be subjected to several absorption/desorption cycles to study its life-cycle stability. The following conditions were employed: absorption was performed under 25 bar H_2 final pressure at 25 °C, while desorption was carried out by heating at 400 °C under dynamic vacuum for 12 h. The cycle-life stability was assessed in terms of kinetics, reversible capacity, and structural modifications during 10 cycles. Figure 8 plots the kinetic curves recorded every second cycle during the absorption step (a) and the reversible capacity during cycling (b).
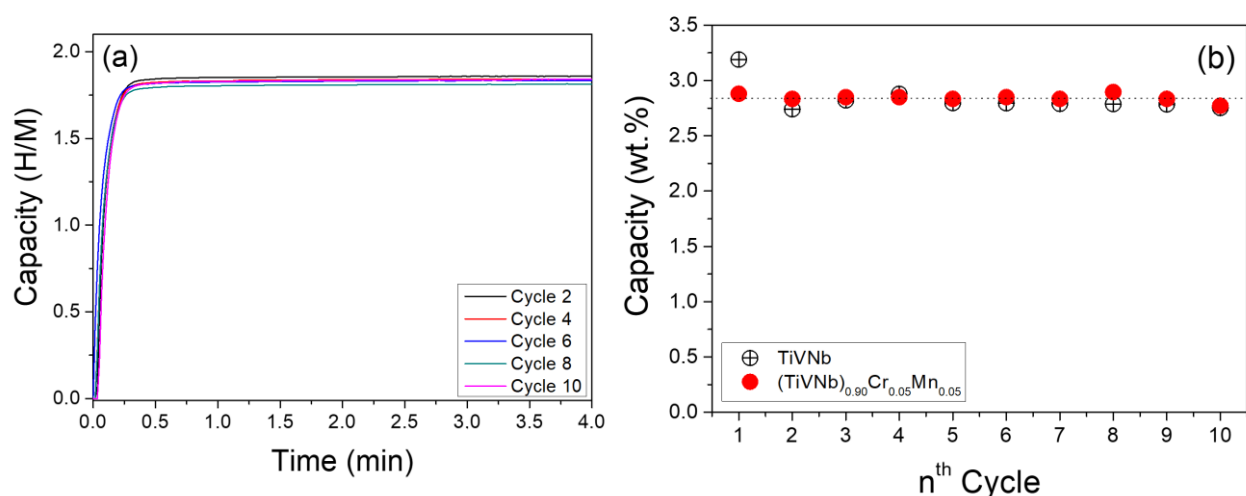

Figure 8. (**a**) The kinetic curves recorded every second cycle during the absorption step under 25 bar and 25 °C. (**b**) The reversible capacity (wt.%) during 10 cycles. For the sake of comparison, the results obtained for the TiVNb alloy are also shown in [34]. The mean value at 2.8 wt.% is plotted as a dotted line.

The kinetic curves are comparable, with very fast reaction rates and full hydrogenation within 1 min at room temperature. The reversible capacity is extremely stable, with a mean value of 2.8 wt.% (1.84 H/M) during cycling and comparable to the pristine TiVNb alloy [34]. The XRD diffraction patterns after the first and last cycles are shown in Figure 9. The diffraction peaks from the *fcc* hydride phase are visible without any secondary phase after cycling. The lattice parameters are similar after the first and last cycles: 4.429(1) Å and 4.441(1) Å, respectively. The only noticeable change in the XRD is the broadening of the peaks after cycling, which points out the formation of defects such as vacancies and dislocations during cycling. This can be related to the stresses developed during the *bcc* ↔ *fcc* phase transformation with a large mismatch between the lattice volumes, as proposed

earlier in the TiVNbCr alloy [24]. In summary, this alloy shows an excellent reversible capacity, one of the most promising values reported, and a stable chemical composition and crystalline structure without phase segregation.
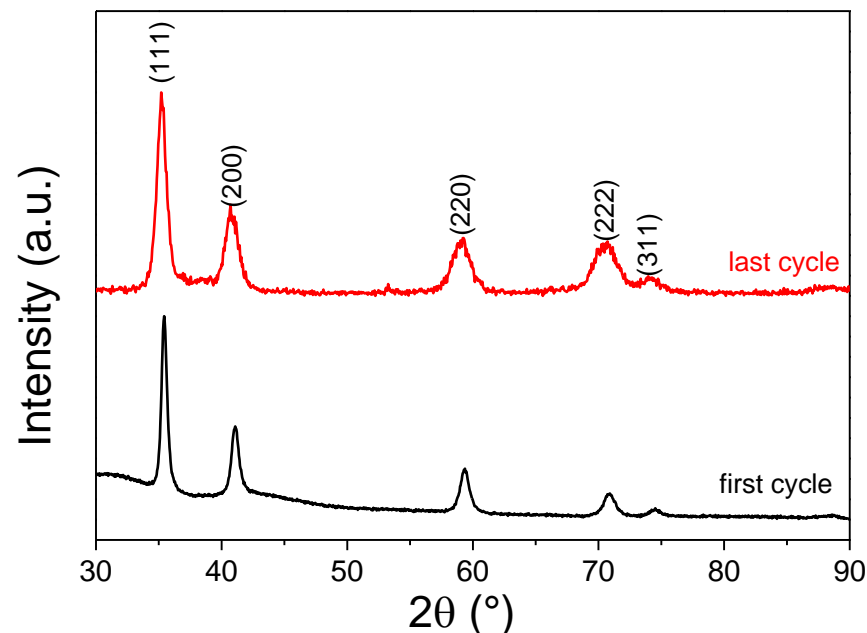

Figure 9. XRD patterns of the *fcc* hydride phase after the first and last absorption cycles ($\lambda = 1.5406$ Å).

4. Conclusions

The single-phase *bcc* $(TiVNb)_{0.90}Cr_{0.05}Mn_{0.05}$ alloy was prepared by arc melting with a dendritic microstructure typical for as-cast HEAs prepared by this method. After an activation procedure at high temperature (350 °C, 3 h), the alloy absorbs hydrogen very fast at room temperature and forms a *fcc* dihydride with a high total hydrogen capacity (~2 H/M). The hydrogen atoms are occupying the tetrahedral interstitial sites of the *fcc* lattice. The hydride was found to be less stable than the pristine TiVNb alloy, pointing out a thermodynamic destabilization by the concomitant addition of 5 at.% Cr and 5 at.% Mn.

The desorption from the *fcc* phase (either hydrogen or deuterium) was studied by in situ synchrotron XRD and neutron diffraction during constant heating. Interestingly, due to different probe beam–matter interactions, synchrotron radiation, and neutrons, they reveal complementary information, i.e., the metallic and deuterium subnetworks, respectively. During desorption from the *fcc* phase, deuterium atoms are well ordered in the tetrahedral sites and start to desorb above 15 °C, whereas they are randomly distributed beyond 260 °C. Above 350 °C, the *fcc* phase completely disappears. Both experiments agreed well and put forward a reversible phase transformation *fcc* → *bcc* that recovers the initial *bcc* phase, while the H/D subnetwork undergoes an order → disorder transition.

This result allowed us to evaluate the absorption/desorption cycling properties. Kinetics are very fast at room temperature, with full absorption in less than 1 min, irrespective of cycle. The alloy shows a stable, high total capacity of 2.8 wt.% during cycling and a stable chemical composition and crystalline structure without phase segregation. It should be noted that the usable capacity under modest desorption conditions is only half that of the dihydride-to-monohydride transition.

Thus, the design strategy consisting of the addition of a small amount of transition metals allows for the obtaining of less stable hydride phases in the very promising TiVNb-based system with very good cycling properties and one of the most interesting reversible capacities in the HEAs foreseen for hydrogen storage.

References

1. Rivard, E.; Trudeau, M.; Zaghib, K. Hydrogen Storage for Mobility: A Review. *Materials* **2019**, *12*, 1973. [CrossRef]
2. Eberle, U.; Felderhoff, M.; Schuth, F. Chemical and Physical Solutions for Hydrogen Storage. *Angew. Chem.-Int. Edit.* **2009**, *48*, 6608–6630. [CrossRef]
3. Abe, J.O.; Popoola, A.P.I.; Ajenifuja, E.; Popoola, O.M. Hydrogen Energy, Economy and Storage: Review and Recommendation. *Int. J. Hydrogen Energy* **2019**, *44*, 15072–15086. [CrossRef]
4. Lebrouhi, B.E.; Djoupo, J.J.; Lamrani, B.; Benabdelaziz, K.; Kousksou, T. Global Hydrogen Development—A Technological and Geopolitical Overview. *Int. J. Hydrogen Energy* **2022**, *47*, 7016–7048. [CrossRef]
5. Borgschulte, A. The Hydrogen Grand Challenge. *Front. Energy Res.* **2016**, *4*, 11. [CrossRef]
6. Hirscher, M.; Yartys, V.A.; Baricco, M.; Bellosta von Colbe, J.; Blanchard, D.; Bowman, R.C.; Broom, D.P.; Buckley, C.E.; Chang, F.; Chen, P.; et al. Materials for Hydrogen-Based Energy Storage—Past, Recent Progress and Future Outlook. *J. Alloys Compd.* **2020**, *827*, 153548. [CrossRef]
7. Crivello, J.-C.; Dam, B.; Denys, R.V.; Dornheim, M.; Grant, D.M.; Huot, J.; Jensen, T.R.; de Jongh, P.; Latroche, M.; Milanese, C.; et al. Review of Magnesium Hydride-Based Materials: Development and Optimisation. *Appl. Phys. A-Mater. Sci. Process.* **2016**, *122*, 97. [CrossRef]
8. Miracle, D.B.; Senkov, O.N. A Critical Review of High Entropy Alloys and Related Concepts. *Acta Mater.* **2017**, *122*, 448–511. [CrossRef]
9. Miracle, D.B. High Entropy Alloys as a Bold Step Forward in Alloy Development. *Nat. Commun.* **2019**, *10*, 1805. [CrossRef] [PubMed]
10. Senkov, O.N.; Miracle, D.B.; Chaput, K.J.; Couzinie, J.-P. Development and Exploration of Refractory High Entropy Alloys—A Review. *J. Mater. Res.* **2018**, *33*, 3092–3128. [CrossRef]
11. Gao, M.C.; Miracle, D.B.; Maurice, D.; Yan, X.; Zhang, Y.; Hawk, J.A. High-Entropy Functional Materials. *J. Mater. Res.* **2018**, *33*, 3138–3155. [CrossRef]
12. Wang, Z.; Chen, S.; Yang, S.; Luo, Q.; Jin, Y.; Xie, W.; Zhang, L.; Li, Q. Light-Weight Refractory High-Entropy Alloys: A Comprehensive Review. *J. Mater. Sci. Technol.* **2023**, *151*, 41–65. [CrossRef]
13. Karlsson, D.; Ek, G.; Cedervall, J.; Zlotea, C.; Møller, K.T.; Hansen, T.C.; Bednarčík, J.; Paskevicius, M.; Sørby, M.H.; Jensen, T.R.; et al. Structure and Hydrogenation Properties of a HfNbTiVZr High-Entropy Alloy. *Inorg. Chem.* **2018**, *57*, 2103–2110. [CrossRef]
14. Nygård, M.M.; Ek, G.; Karlsson, D.; Sørby, M.H.; Sahlberg, M.; Hauback, B.C. Counting Electrons—A New Approach to Tailor the Hydrogen Sorption Properties of High-Entropy Alloys. *Acta Mater.* **2019**, *175*, 121–129. [CrossRef]
15. Nygård, M.M.; Sławiński, W.A.; Ek, G.; Sørby, M.H.; Sahlberg, M.; Keen, D.A.; Hauback, B.C. Local Order in High-Entropy Alloys and Associated Deuterides—A Total Scattering and Reverse Monte Carlo Study. *Acta Mater.* **2020**, *199*, 504–513. [CrossRef]
16. Nygård, M.M.; Fjellvåg, Ø.S.; Sørby, M.H.; Sakaki, K.; Ikeda, K.; Armstrong, J.; Vajeeston, P.; Sławiński, W.A.; Kim, H.; Machida, A.; et al. The Average and Local Structure of TiVCrNbDx (X = 0,2.2,8) from Total Scattering and Neutron Spectroscopy. *Acta Mater.* **2021**, *205*, 116496. [CrossRef]
17. Nygård, M.M.; Ek, G.; Karlsson, D.; Sahlberg, M.; Sørby, M.H.; Hauback, B.C. Hydrogen Storage in High-Entropy Alloys with Varying Degree of Local Lattice Strain. *Int. J. Hydrogen Energy* **2019**, *44*, 29140–29149. [CrossRef]

18. Yang, F.; Wang, J.; Zhang, Y.; Wu, Z.; Zhang, Z.; Zhao, F.; Huot, J.; Grobivć Novaković, J.; Novaković, N. Recent Progress on the Development of High Entropy Alloys (HEAs) for Solid Hydrogen Storage: A Review. *Int. J. Hydrogen Energy* **2022**, *47*, 11236–11249. [CrossRef]

19. Pedroso, O.A.; Botta, W.J.; Zepon, G. An Open-Source Code to Calculate Pressure-Composition-Temperature Diagrams of Multicomponent Alloys for Hydrogen Storage. *Int. J. Hydrogen Energy* **2022**, *47*, 32582–32593. [CrossRef]

20. Ponsoni, J.B.; Aranda, V.; da Silva Nascimento, T.; Strozi, R.B.; Botta, W.J.; Zepon, G. Design of Multicomponent Alloys with C14 Laves Phase Structure for Hydrogen Storage Assisted by Computational Thermodynamic. *Acta Mater.* **2022**, *240*, 118317. [CrossRef]

21. Zepon, G.; Silva, B.H.; Zlotea, C.; Botta, W.J.; Champion, Y. Thermodynamic Modelling of Hydrogen-Multicomponent Alloy Systems: Calculating Pressure-Composition-Temperature Diagrams. *Acta Mater.* **2021**, *215*, 117070. [CrossRef]

22. Strozi, R.B.; Leiva, D.R.; Zepon, G.; Botta, W.J.; Huot, J. Effects of the Chromium Content in (TiVNb)100−xCrx Body-Centered Cubic High Entropy Alloys Designed for Hydrogen Storage Applications. *Energies* **2021**, *14*, 3068. [CrossRef]

23. Strozi, R.B.; Silva, B.H.; Leiva, D.R.; Zlotea, C.; Botta, W.J.; Zepon, G. Tuning the Hydrogen Storage Properties of Ti-V-Nb-Cr Alloys by Controlling the Cr/(TiVNb) Ratio. *J. Alloys Compd.* **2023**, *932*, 167609. [CrossRef]

24. Strozi, R.B.; Witman, M.; Stavila, V.; Cizek, J.; Sakaki, K.; Kim, H.; Melikhova, O.; Perrière, L.; Machida, A.; Nakahira, Y.; et al. Elucidating Primary Degradation Mechanisms in High-Cycling-Capacity, Compositionally Tunable High-Entropy Hydrides. *ACS Appl. Mater. Interfaces* **2023**, *15*, 38412–38422. [CrossRef] [PubMed]

25. Ferreira, T.; Pineda-Romero, N.; Botta, W.J.; Zepon, G.; Zlotea, C. Tuning the Hydride Stability of the TiVNb-Based Alloys by Equimolar Cr/Al Addition. *Intermetallics* **2023**, *161*, 107992. [CrossRef]

26. Pineda-Romero, N.; Zlotea, C. Uncovering the Effect of Al Addition on the Hydrogen Storage Properties of the Ternary TiVNb Alloy. *Materials* **2022**, *15*, 7974. [CrossRef]

27. Serrano, L.; Moussa, M.; Yao, J.-Y.; Silva, G.; Bobet, J.-L.; Santos, S.F.; Cardoso, K.R. Development of Ti-V-Nb-Cr-Mn High Entropy Alloys for Hydrogen Storage. *J. Alloys Compd.* **2023**, *945*, 169289. [CrossRef]

28. Rodriguezcarvajal, J. Recent advances in magnetic-structure determination by neutron powder diffraction. *Physica B* **1993**, *192*, 55–69. [CrossRef]

29. Le Bail, A.; Duroy, H.; Fourquet, J.L. Ab-Initio Structure Determination of LiSbWO6 by X-Ray Powder Diffraction. *Mater. Res. Bull.* **1988**, *23*, 447–452. [CrossRef]

30. Cheary, R.W.; Coelho, A.A.; Cline, J.P. Fundamental Parameters Line Profile Fitting in Laboratory Diffractometers. *J. Res. Natl. Inst. Stand. Technol.* **2004**, *109*, 1. [CrossRef]

31. Coelho, A.A. TOPAS and TOPAS-Academic: An Optimization Program Integrating Computer Algebra and Crystallographic Objects Written in C++. *J. Appl. Cryst.* **2018**, *51*, 210–218. [CrossRef]

32. Gross, K.J.; Hardy, B.; Parilla, P.A. *Recommended Best Practices for Characterizing Engineering Properties of Hydrogen Storage Materials*; National Renewable Energy Laboratory: Golden, CO, USA, 2013.

33. Gordon, A.; Tristan, F. SI Chemical Data, 3rd Edition. *J. Chem. Educ.* **1995**, *72*, A109. [CrossRef]

34. Pineda-Romero, N.; Witman, M.; Stavila, V.; Zlotea, C. The Effect of 10 at.% Al Addition on the Hydrogen Storage Properties of the $Ti_{0.33}V_{0.33}Nb_{0.33}$ Multi-Principal Element Alloy. *Intermetallics* **2022**, *146*, 107590. [CrossRef]

35. Pineda Romero, N.; Witman, M.; Harvey, K.; Stavila, V.; Nassif, V.; Elkaïm, E.; Zlotea, C. Large Destabilization of (TiVNb)-Based Hydrides via (Al, Mo) Addition: Insights from Experiments and Data-Driven Models. *ACS Appl. Energy Mater.* **2023**, *6*, 12560–12572. [CrossRef]

36. Couzinié, J.P.; Dirras, G.; Perrière, L.; Chauveau, T.; Leroy, E.; Champion, Y.; Guillot, I. Microstructure of a Near-Equimolar Refractory High-Entropy Alloy. *Mater. Lett.* **2014**, *126*, 285–287. [CrossRef]

37. Nakano, K.; Narumi, T.; Morishita, K.; Yasuda, H. Characterization of Growing Dendrites in CrMnFeCoNi High-Entropy Alloy by Time-Resolved and *In-Situ* Tomography. *Mater. Trans.* **2020**, *61*, 596–604. [CrossRef]

38. Feng, R.; Gao, M.C.; Lee, C.; Mathes, M.; Zuo, T.; Chen, S.; Hawk, J.A.; Zhang, Y.; Liaw, P.K. Design of Light-Weight High-Entropy Alloys. *Entropy* **2016**, *18*, 333. [CrossRef]

39. Marques, F.; Balcerzak, M.; Winkelmann, F.; Zepon, G.; Felderhoff, M. Review and Outlook on High-Entropy Alloys for Hydrogen Storage. *Energy Environ. Sci.* **2021**, *14*, 5191–5227. [CrossRef]

40. Somo, T.R.; Lototskyy, M.V.; Yartys, V.A.; Davids, M.W.; Nyamsi, S.N. Hydrogen Storage Behaviours of High Entropy Alloys: A Review. *J. Energy Storage* **2023**, *73*, 108969. [CrossRef]

41. Silva, B.H.; Zlotea, C.; Champion, Y.; Botta, W.J.; Zepon, G. Design of TiVNb-(Cr, Ni or Co) Multicomponent Alloys with the Same Valence Electron Concentration for Hydrogen Storage. *J. Alloys Compd.* **2021**, *865*, 158767. [CrossRef]